Monthly Notices
of the
ROYAL ASTRONOMICAL SOCIETY

MNRAS **433,** 434–444 (2013)
Advance Access publication 2013 May 21

doi:10.1093/mnras/stt738

Searching for nuclear stellar discs in simulations of star cluster mergers

E. Portaluri,[1⋆] E. M. Corsini,[1,2] L. Morelli,[1,2] M. Hartmann,[3] E. Dalla Bontà,[1,2] Victor P. Debattista[4] and A. Pizzella[1,2]

[1]*Dipartimento di Fisica e Astronomia 'G. Galilei', Università di Padova, vicolo dell'Osservatorio 3, I-35122 Padova, Italy*
[2]*INAF–Osservatorio Astronomico di Padova, vicolo dell'Osservatorio 5, I-35122 Padova, Italy*
[3]*Astronomisches Rechen-Institut, Zentrum für Astronomie der Universität Heidelberg (ZAH), Mönchhofstraße 12-14, D-69120 Heidelberg, Germany*
[4]*Jeremiah Horrocks Institute, University of Central Lancashire, Preston PR1 2HE, UK*

Accepted 2013 April 26. Received 2013 April 26; in original form 2013 February 4

ABSTRACT

The nuclei of galaxies often host small stellar discs with scalelengths of a few tens of parsecs and luminosities up to 10^7 $L_\odot$. To investigate the formation and properties of nuclear stellar discs (NSDs), we look for their presence in a set of *N*-body simulations studying the dissipationless merging of multiple star clusters in galactic nuclei. A few tens of star clusters with sizes and masses comparable to those of globular clusters observed in the Milky Way are accreted on to a pre-existing nuclear stellar component: either a massive super star cluster or a rapidly rotating, compact disc with a scalelength of a few parsecs, mimicking the variety of observed nuclear structures. Images and kinematic maps of the simulation time-steps are then built and analysed as if they were real and at the distance of the Virgo cluster. We use the Scorza–Bender method to search for the presence of disc structures via photometric decomposition. In one case, the merger remnant has all the observed photometric and kinematic properties of NSDs observed in real galaxies. This shows that current observations are consistent with most of the NSD mass being assembled from the migration and accretion of star clusters into the galactic centre. In the other simulation instead, we detect an elongated structure from the unsharp masked image, that does not develop the photometric or kinematic signature of an NSD. Thus, in the context of searches for a disc structure, the Scorza–Bender method is a robust and necessary tool.

Key words: galaxies: evolution – galaxies: formation – galaxies: kinematics and dynamics – galaxies: nuclei – galaxies: photometry – galaxies: structure.

1 INTRODUCTION

The nuclei of galaxies occupy a privileged position at the bottom of the galactic potential well. Thus, the morphology, dynamics, star formation and chemical enrichment provide important insight into the evolutionary history of galaxies. Indeed galactic nuclei record the history of the material, whether coming from neighbouring galactic regions or accreted through mergers, that has sunk to the dynamical centre over the lifetime of the parent system.

Due to its superb spatial resolution, the *Hubble Space Telescope (HST)* has been used extensively to image the nuclei of nearby galaxies. Numerous surveys have been carried out to investigate their structure on scales of 10–100 pc over a wide range of morphological types. *HST* imaging has shown that about 20 per cent of elliptical (Ledo et al. 2010) and spiral galaxies (Pizzella et al. 2002) host a nuclear stellar disc (NSD). NSDs are smaller (scalelengths $h \sim$ 10–50 pc) and brighter ($\mu^0_{0,V} \sim 16 - 19$ mag arcsec^{-2}) than embedded discs in early-type galaxies (Scorza & Bender 1995), but they never dominate the light distribution of the galactic nuclei, and locally contribute at most half the galaxy surface brightness. Interestingly, independent of the Hubble type of their host galaxy, NSDs seem to follow the same relation between the central surface brightness and scalelength as the main discs of lenticular and spiral galaxies and as the embedded discs of early-type galaxies (van den Bosch 1998).

Various methods have been used to detect NSDs. The simplest, and therefore traditional, method is the unsharp mask technique to recover non-circular structures in an image. Alternatively, the Scorza–Bender method (Scorza & Bender 1995) recovers the basic structural properties of an NSD (central surface brightness, I_0, and the scalelength radius, h, inclination, i, and major axis position angle, PA) by subtracting from the image the best exponential disc model, which is generally assumed to be perfectly thin.

NSDs have received attention primarily as probes of the mass distribution since they permit measurement of the mass of central supermassive black holes (SBHs) through observation of their stellar kinematics (e.g. van den Bosch & de Zeeuw 1996; Cretton

⋆E-mail: elisa.portaluri@studenti.unipd.it

& van den Bosch 1999; Magorrian 1999). However, the study of NSDs can also advance our understanding of galaxy formation and evolution since their formation and destruction reflects the assembly history of their host galaxies. For example, being dynamically cool systems, NSDs are fragile and do not survive a major merger. Especially in the presence of SBHs of comparable mass, they would be significantly affected by the interaction with a second SBH carried by the merging galaxy (Ledo et al. 2010). Therefore, the age of an NSD constrains the epoch of the last major merger of the host galaxy.

Different mechanisms have been proposed to explain how NSDs form. The capture of external gas accounts for the origin of the counter-rotating NSD in NGC 4458 (Morelli et al. 2004, 2010). Indeed, the presence of a kinematically decoupled component is usually interpreted as the signature of gas accretion or merging of satellite galaxies (Bertola & Corsini 1999). An external origin is also invoked for the gas which formed the stars of the nuclear disc in the early-type spiral NGC 4698, which is rotating perpendicularly with respect to the main galactic disc (Bertola et al. 1999; Pizzella et al. 2002; Corsini et al. 1999, 2012). The secular infall of gas, perhaps via a barred potential, is an alternative way to funnel pre-enriched material into the galactic centre where it accumulates, dissipates and forms stars. This scenario provides a natural explanation for the presence of NSDs in barred galaxies (e.g. NGC 7332, Seifert & Scorza 1996; Falcón-Barroso et al. 2004). In some cases, a bar may even be destroyed in the process, as has been proposed for NGC 4570 (Scorza & van den Bosch 1998; van den Bosch & Emsellem 1998; van den Bosch, Jaffe & van der Marel 1998; Krajnović & Jaffe 2004; Morelli et al. 2010) and NGC 4621 (Sil'chenko 1997).

Examples of on-going formation via dissipation include the NSDs in NGC 5845 (Kormendy et al. 1994) and in NGC 4486A (Kormendy et al. 2005). However, other NSDs are as old as the main body of the host galaxy (NGC 4128, Krajnović & Jaffe 2004; NGC 4342, van den Bosch et al. 1998; NGC 4458, Morelli et al. 2004; NGC 4621, Krajnović & Jaffe 2004; NGC 4698, Corsini et al. 2012). The stellar populations in NSDs have been studied in detail in only a few more objects. In NGC 4478, the NSD is younger, more metal rich and less overabundant than the rest of the galaxy (Morelli et al. 2004). In contrast, the NSD of NGC 5308 is made of a younger and more metal-poor stellar population than the host galaxy (Krajnović & Jaffe 2004). Both the NSD and bulge of NGC 4570 show an intermediate-age stellar population although the NSD is more metal rich (Krajnović & Jaffe 2004).

In some cases an NSD coexists with a massive and dense nuclear star cluster with typical $L_V \sim 10^6$–10^7 $L_\odot$ and effective radius of a few parsecs. These objects are observed in the centre of both early-type (e.g. NGC 4458, NGC 4478 and NGC 4570, Ferrarese et al. 2006; Ledo et al. 2010) and late-type galaxies (e.g. NGC 4206, Seth et al. 2006).

Despite recent progress, no satisfying explanation has been provided for the deposition of the high gas densities that are needed to enable an in situ formation of nuclear star clusters (Shlosman & Begelman 1989; Milosavljević 2004; Bekki 2007; Emsellem & van de Ven 2008). An alternative scenario for the build-up of nuclear star clusters is the dissipationless coalescence of star clusters sinking to the bottom of the potential well by dynamical friction (Tremaine, Ostriker & Spitzer 1975; Capuzzo-Dolcetta 1993; Lotz et al. 2001; Capuzzo-Dolcetta & Miocchi 2008a,b; Antonini et al. 2012; Antonini 2013). Agarwal & Milosavljević (2011) showed that the rate at which the nuclear star cluster grows by accreting young star clusters depends on their formation rate, migration time and dissolution time. The resulting compact nuclear star cluster is embedded in a more extended and diffuse component resembling a small pseudo-bulge. The size of such a disc-like structure in models including the prompt dissolution of star clusters matches that of the observed NSDs. This opens the possibility that NSDs may be forming via star cluster accretion. In addition, the observed scaling relations between the nuclear star cluster masses and the velocity dispersion of their host spheroids and between the sizes of nuclear star clusters and their luminosities can be explained by a dissipationless scenario (Antonini 2013).

Some nuclear star clusters have a complex structure possessing both a spheroidal component and an elongated ring or disc component with a scalelength of a few parsecs (Seth et al. 2006, 2008). Hartmann et al. (2011, hereafter H11) and De Lorenzi et al. (2013) found that no more than half the mass of the multicomponent nuclear star cluster in NGC 4244 could have been assembled in star clusters that migrated and merged at the centre of the galaxy. They concluded that the rest of the nuclear star cluster mass must have been produced by in situ star formation. In this paper, we analyse some of the *N*-body simulations of H11 to look for the presence of an NSD and to test whether the dissipationless merger of star clusters is a viable scenario for the formation and growth of NSDs (as opposed to nuclear star clusters). The details of the simulations are given in Section 2. Section 3 describes the analysis of their photometric and kinematic properties based on mock images and kinematic maps of the simulated galaxies (Section 3.1), including the search for NSDs (Section 3.2), the measurement of their structural properties using the Scorza–Bender method (Section 3.3), and the computation of the rotation parameter (Section 3.4). Results and conclusions are discussed in Sections 4 and 5, respectively.

2 SIMULATIONS

The simulations used here have been presented already in H11. Here, therefore we provide only a brief description of the simulations and refer the reader to H11 for more details. The two simulations we use are referred to as A1 and A2 in H11 and we continue to refer to them as such here.

We are interested in the evolution in the inner ∼100 pc of galaxies; we therefore neglect the dark matter halo. Both simulations live at the centre of a Hernquist (1990) bulge:

$$\rho(r) = \frac{a M_\mathrm{b}}{2\pi r\,(r+a)^3}, \tag{1}$$

where M_b is the bulge mass and a is the scale radius. We use $M_\mathrm{b} = 5 \times 10^9$ $M_\odot$ and $a = 1.7$ kpc. The bulge is populated by 3.5×10^6 particles with masses ranging from 40 $M_\odot$ at the centre to 3.9×10^5 $M_\odot$ further out (Sellwood 2008); their softening is related to their mass via $\epsilon_p \propto m_p^{1/3}$, as shown in fig. 8 of H11.

We set up model star clusters, ranging in mass from 2×10^5 $M_\odot$ to 2×10^6 $M_\odot$, using the isotropic distribution function of a lowered polytrope with index $n = 2$:

$$f(x, v) \propto [-2E(x, v)]^{1/2} - [-2E_\mathrm{max}]^{1/2}, \tag{2}$$

where (x, v) are the phase space coordinates, and E is the energy. This distribution function reproduces well the core profile of observed star clusters, as shown in fig. 9 of H11. We produce equilibrium models via the iterative procedure described in Debattista & Sellwood (2000). We set up three such models, C3–C5, using the naming scheme of H11. Star cluster models have all particles (4×10^5 for C3 model and 4×10^4 for C4–C5) of equal mass

Table 1. Star clusters used in the simulations.

Model	M_* ($M_\odot$)	R_e (pc)	c
C3	2.0×10^6	2.18	0.12
C4	2.0×10^5	1.11	0.12
C5	6.0×10^5	1.11	0.16

Note. Column (2): stellar mass. Column (3): half-mass radius. Column (4): concentration parameter.

($5.0\,M_\odot$ for C3–C4 and $15\,M_\odot$ for C5) and equal softening ($\epsilon = 0.13$ pc). No black holes have been included in the star cluster models. Table 1 lists the properties of the star cluster models. The concentration c is defined as $c \equiv \log(R_e/R_c)$ where R_e is the half-mass radius and R_c is the core radius, where the surface density drops to half of the central. The masses and sizes of the star clusters are comparable to young massive star clusters in the Milky Way (Figer, McLean & Morris 1999; Figer et al. 2002).

The initial model in run A1 consists of the bulge hosting a nuclear cluster spheroid (NCS), produced by letting star cluster C3 fall to the centre starting from a circular orbit at 127 pc. We use model C5 for the accreted star clusters, starting them on circular orbits at a distance of 32 pc from the centre. Each accretion is allowed to finish before a new star cluster is inserted. In total 27 star clusters, corresponding to 8.1 times the NCS's initial mass, are accreted in 810 Myr.

In model A2, we generated a bare nuclear cluster disc (NCD) model by adiabatically growing an exponential disc with a scale-length $R_d = 9.5$ pc and mass of $1 \times 10^6\,M_\odot$ at the centre of the bulge model. We set Toomre-$Q = 1.2$, as described in Debattista & Sellwood (2000). In this model we accrete, over 1.8 Gyr, 50 copies of model C4 sequentially on circular orbits, each starting 63 pc from the centre. This corresponds to 10 times the NCD's initial mass.

3 ANALYSIS

3.1 Pseudo surface photometry and stellar kinematics

We consider three outputs from each run: in model A1 after the accretion of 10, 20 and 27 star clusters and in model A2 after the accretion of 10, 30 and 50 star clusters. We start by building an *I*-band image for each simulation time-step. We model the luminosity distribution of each galaxy component from its mass distribution by adopting M/L ratios from Maraston (1998, 2005):

(i) for the NCS of model A1, we assume two different stellar components with the same mass:

(a) a young stellar population with an age 1 Gyr, a metallicity [Fe/H] = − 0.4 dex and $(M/L)_I = 0.52\,M_\odot/L_\odot$;
(b) an old stellar population with an age 10 Gyr, a metallicity [Fe/H] = −1.4 dex and with $(M/L)_I = 2.70\,M_\odot/L_\odot$;

(ii) for the initial NCD of model A2, we adopt a stellar population with $(M/L)_I = 0.20\,M_\odot/L_\odot$ corresponding to an age of 70 Myr and a metallicity of [Fe/H] = − 0.4 dex;
(iii) for the host bulge in both model A1 and A2, we consider the same population as the old part of the NCS;
(iv) in each time-step of both model A1 and A2, we consider the same mixed population of the NCS for all the star clusters except for the last accreted one, for which we adopt the same young population as the NCD.

These ages and metallicities are chosen to match the properties of the stellar components observed in the nucleus of NGC 4244 (Seth et al. 2006) as in H11. During the evolution time, we consider that all the components become older, reaching the same mixed population as the NCS, except for the last accreted star cluster, for which we adopt the M/L ratio described above. In order to increase the resolution at the centre of the model, particles in the bulge model have different masses depending on their total angular momentum; at larger radii particles have masses as large as $3.9 \times 10^5\,M_\odot$. Since these project on to the nucleus, in our analysis of projected quantities we exclude all bulge particles beyond 200 pc from the galaxy centre.

We generate images assuming the Virgo Cluster distance, 16 Mpc. Therefore, the angular size of 1 arcsec corresponds to 77.6 pc. Images of the different time-steps are trimmed to match the field of view (162×162 arcsec^2) of the ultraviolet and visible channel (UVIS) of the Wide Field Camera 3 (WFC3) on board the *HST*, with a pixel scale of 0.04 arcsec pixel^{-1}, and gain and readout noise set to 1.5 e$^-$ count^{-1} and 3.0 e$^-$ rms, respectively (Dressel 2011). Finally, a background level and photon noise are added to the resulting images to yield a signal-to-noise ratio similar to that of the *HST* images of galaxy nuclei hosting an NSD. Given that NSDs are easiest to detect when nearly edge-on, the mock images to be analysed are generated by adopting a galaxy inclination of 75° which takes into account the detection limit of embedded discs as a function of their luminosity and inclination (Rix & White 1990).

The luminosity-weighted kinematics of the stars is derived for each simulated galaxy as seen edge-on after excluding the contribution of the bulge to avoid its contamination. The resulting maps of the line-of-sight velocity and velocity dispersion are shown in Fig. 1. As pointed out by H11, the measured kinematics are dominated by the nuclear star cluster out to 15 pc from the centre. At larger radii ($r \simeq 30$ pc), the amplitude of the stellar rotation ($10 \lesssim V_{max} \lesssim 40$ km s^{-1}) is consistent with kinematic measurements of actual NSDs (e.g. van den Bosch et al. 1998; Bertola et al. 1999; Halliday et al. 2001).

3.2 Detection of the nuclear stellar disc

To test for the presence of an NSD in the mock WFC3/UVIS images of the simulated galaxies, we construct the unsharp masked image of the frames as in Pizzella et al. (2002). Each image is divided by itself after convolution with a circular Gaussian of width $\sigma = 2$, 6, 10 or 20 pixels corresponding to 0.08, 0.024, 0.4 or 0.8 arcsec, respectively (Fig. 2). This procedure enhances any non-circular structure extending over a spatial scale comparable to the smoothing scale. Different values of σ are adopted to identify structures of different sizes. For each model, the location, orientation and size of the elongated nuclear component remain similar in all the time-steps.

Morelli et al. (2004) demonstrated that bright, elongated nuclear structures in unsharp masked images are not an artefact of the image processing. Such structures are always observed in galactic nuclei if an inclined NSD is present. However, the same feature in the unsharp masked images of bulges can also be caused by isophotes of increasing ellipticity inwards. Therefore, to unveil an NSD it is necessary to perform also a detailed measurement of the surface brightness distribution in the nuclear regions. The isophotes of a bulge are expected to be nearly elliptical, even if the ellipticity changes with radius. Instead, the presence of an inclined NSD will

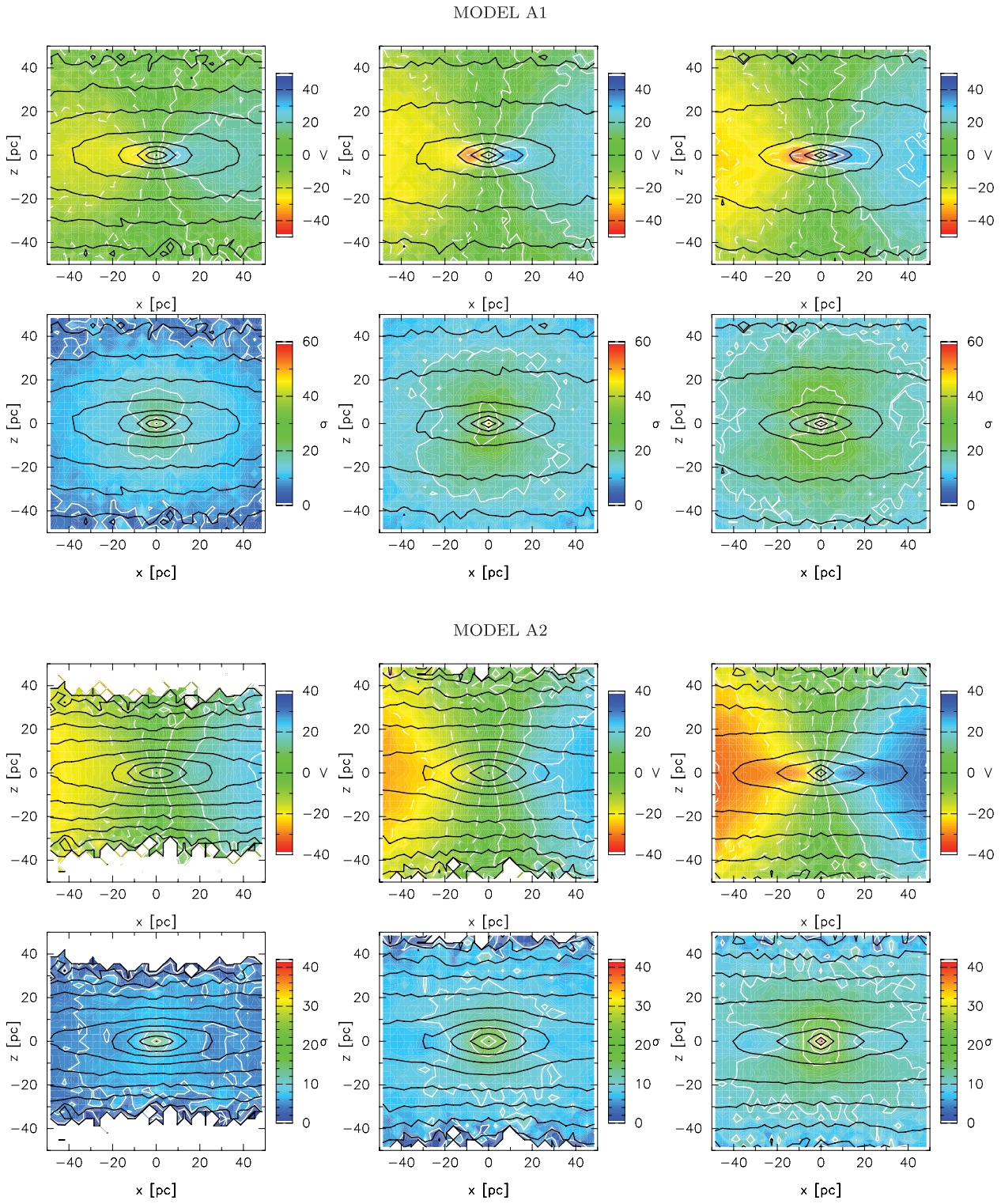

Figure 1. Top panels: line-of-sight stellar velocity (top row) and velocity dispersion (bottom row) maps for the simulated galaxy in model A1 after the accretion of 10 (left-hand panels), 20 (central panels) and 27 star clusters (right-hand panels). The colour code is at the right of each panel. The black contours show the galaxy isophotes at a level of 90, 80, . . . , 10 per cent of the central surface brightness. The white lines show kinematic contours appropriate to each panel. The field of view is 0.65×0.65 arcsec^2 (corresponding to 50×50 pc^2 at the assumed distance). Bottom panels: as above, but for the simulated galaxy in model A2 after the accretion of 10 (left-hand panels), 30 (central panels) and 50 star clusters (right-hand panels).

result in isophotes with a discy shape, due to the superposition of the light contribution of the rounder bulge with that from the more elongated NSD (Scorza & Bender 1995). A sharp increase of the disciness of the innermost isophotes of a galaxy is usually associated with a strong increase of their ellipticity. The peak of both ellipticity and disciness in the same radial range is therefore the full photometric signature of the presence of an NSD embedded in the bulge.

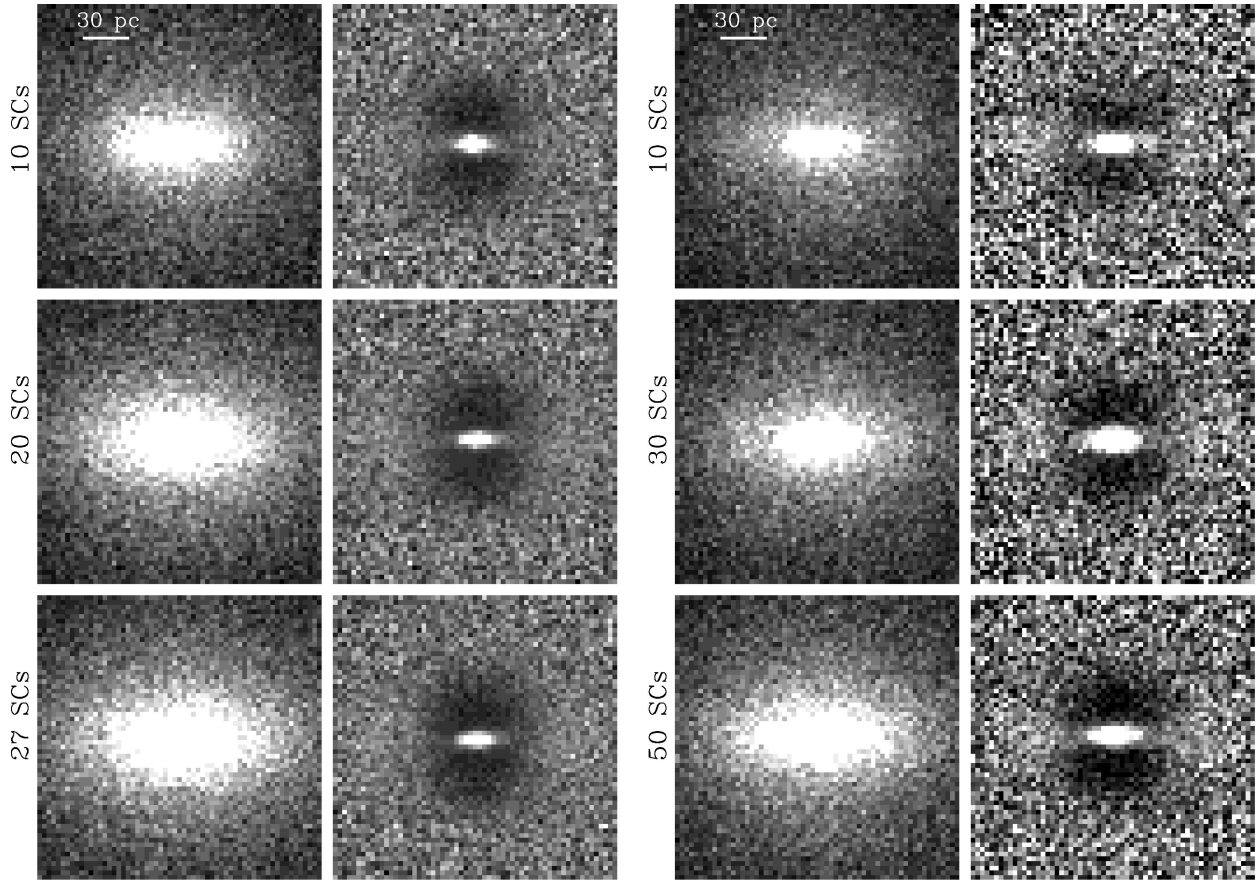

Figure 2. Left: mock WFC3/UVIS *I*-band (left-hand panels) and unsharp masked images (right-hand panels) of model A1 after the accretion of 10 (top panels), 20 (middle panels) and 27 star clusters (bottom panels). The field of view is 2.4×2.4 arcsec^2 (corresponding to 186×186 pc^2) and the image scale is given in the upper-left corner of the first panel. The unsharp masked images were obtained by adopting a smoothing Gaussian of $\sigma = 10$ pixel corresponding to 0.4 arcsec. Right: as on the left, but for model A2 after the accretion of 10 (top panels), 30 (middle panels) and 50 star clusters (bottom panels). These images have been obtained at an inclination of 75°.

We fit isophotes to the model images using the IRAF[1] task ELLIPSE (Jedrzejewski 1987). Isophotes are fitted with ellipses, allowing their centres to vary in order to look for asymmetries in the light distribution. Within the errors of the fits, we find no evidence of variations in the fitted centres. The ellipse fitting is then repeated with the ellipse centres fixed. The resulting azimuthally averaged surface brightness, ellipticity, PA and fourth cosine Fourier coefficient (A_4) profiles are presented in Figs 3 and 4 for models A1 and A2, respectively. Positive values of the A_4 Fourier coefficient are characteristic of discy isophotes (Bender, Doebereiner & Moellenhoff 1988).

The radial profile of ellipticity peaks at about 0.2 arcsec from the centre ($\epsilon_{\rm max} \simeq 0.6$) in all the mock images of model A1. Round isophotes ($\epsilon \simeq 0$) are observed for radii larger than 2 arcsec. Within the innermost 2 arcsec there is no change in the A_4 Fourier coefficient, which is nearly constant and slightly positive ($A_4 \simeq 0.01$ after the accretion of 10 and 20 star clusters, increasing to $A_4 \simeq 0.02$ after the accretion of 27 star clusters). Thus, model A1 never develops the photometric signature of observed NSDs.

In model A2, instead, both the ellipticity and the A_4 Fourier coefficient show a sharp increase within 1.5 arcsec from the centre in all the time-steps. The maximum observed values of ellipticity and disciness are $\epsilon_{\rm max} \simeq 0.6$ and $A_{4,\,\rm max} \simeq 0.05$, respectively. We interpret these photometric features as the signature of an embedded NSD in the bulge of model A2. Indeed the same photometric features are observed in galactic nuclei hosting an NSD (e.g. Scorza & van den Bosch 1998; Krajnović & Jaffe 2004; Morelli et al. 2010).

3.3 Photometric decomposition

We first measure the PA of the major axis of the NSD found in model A2 in order to check whether we can successfully recover the orientation of the NSD. We assume the images are oriented with the North up and East left and analyse them after unsharp masking. The images are rotated from 0° to 179.°8 in steps of 0.°2 and we measure the flux within a horizontal strip of 51×9 pixels crossing the galaxy centre. The maximum flux is measured when the strip is aligned with the NSD major axis. In this way, we find PA $= 90° \pm 2°$, consistent with the input line of nodes of the system.

We then apply a photometric decomposition of the surface brightness based on the Scorza–Bender method (Scorza & Bender 1995), as implemented by Morelli et al. (2004), to the images of model A2. The photometric decomposition, which is performed independently for each time-step, is based on the assumption that both the host bulge and the inclined NSD are each characterized by elliptical isophotes with constant ellipticity. The method consists of an

[1] Imaging Reduction and Analysis Facilities (IRAF) is distributed by the National Optical Astronomy Observatories which are operated by the Association of Universities for Research in Astronomy (AURA) under cooperative agreement with the National Science Foundation.

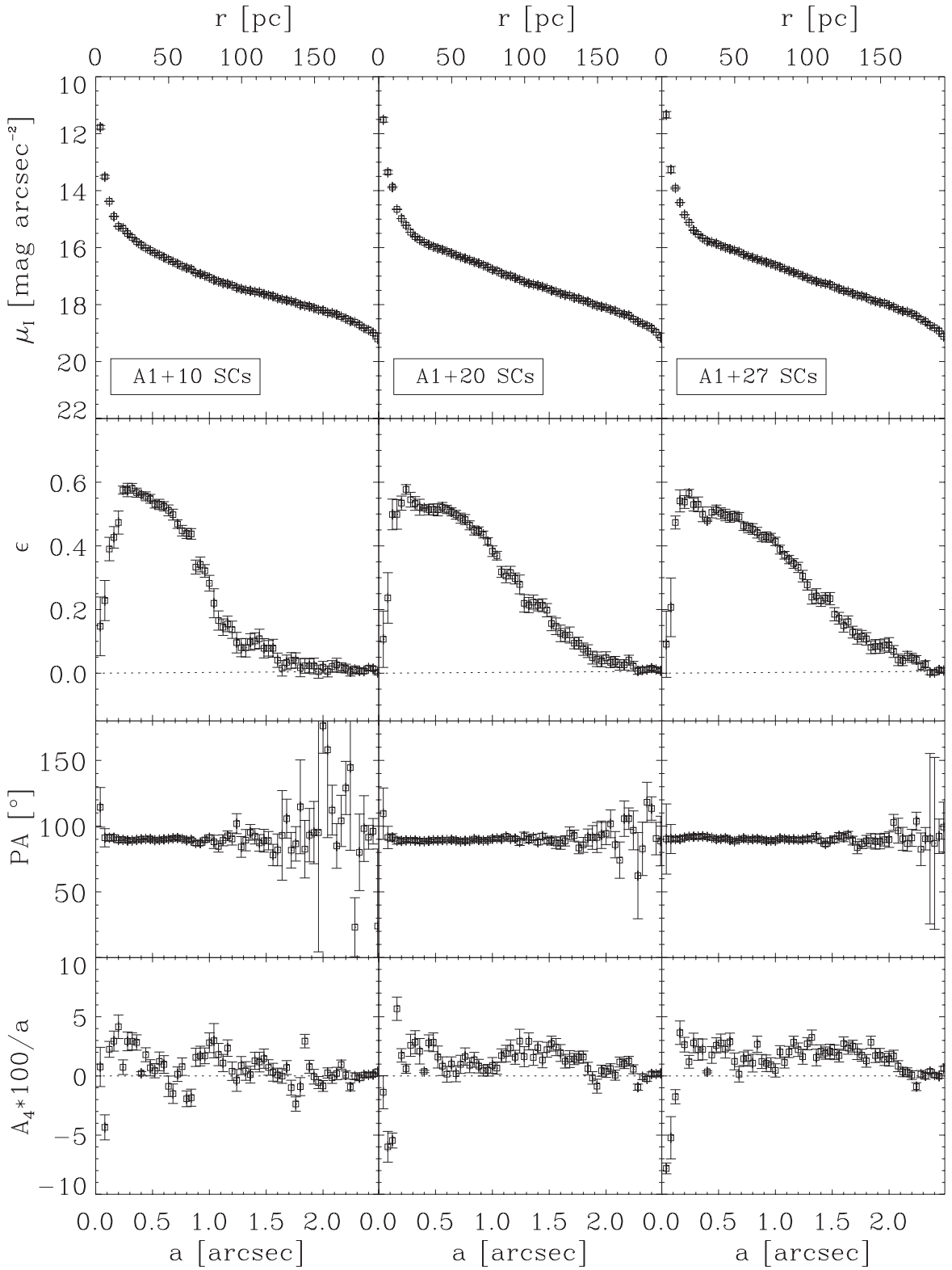

Figure 3. Isophotal parameters of the nuclear region of model A1 as a function of the isophotal semimajor axis based on the analysis of the surface brightness distribution after the accretion of 10 (left-hand panels), 20 (central panels) and 27 (right-hand panels) star clusters. From top to bottom: radial profiles of the surface brightness, ellipticity, PA and fourth cosine Fourier coefficient.

iterative subtraction of different models of an infinitesimally thin exponential disc. The disc has central surface brightness I_0, scale-length h, and apparent axial ratio q. We assume PA = 90° for the PA of the disc major axis.

For real images, it is crucial to first deconvolve the surface brightness distribution from the effects of the *HST* point spread function (PSF) in order to properly derive the photometric parameters of the NSDs (e.g. van den Bosch & Emsellem 1998;

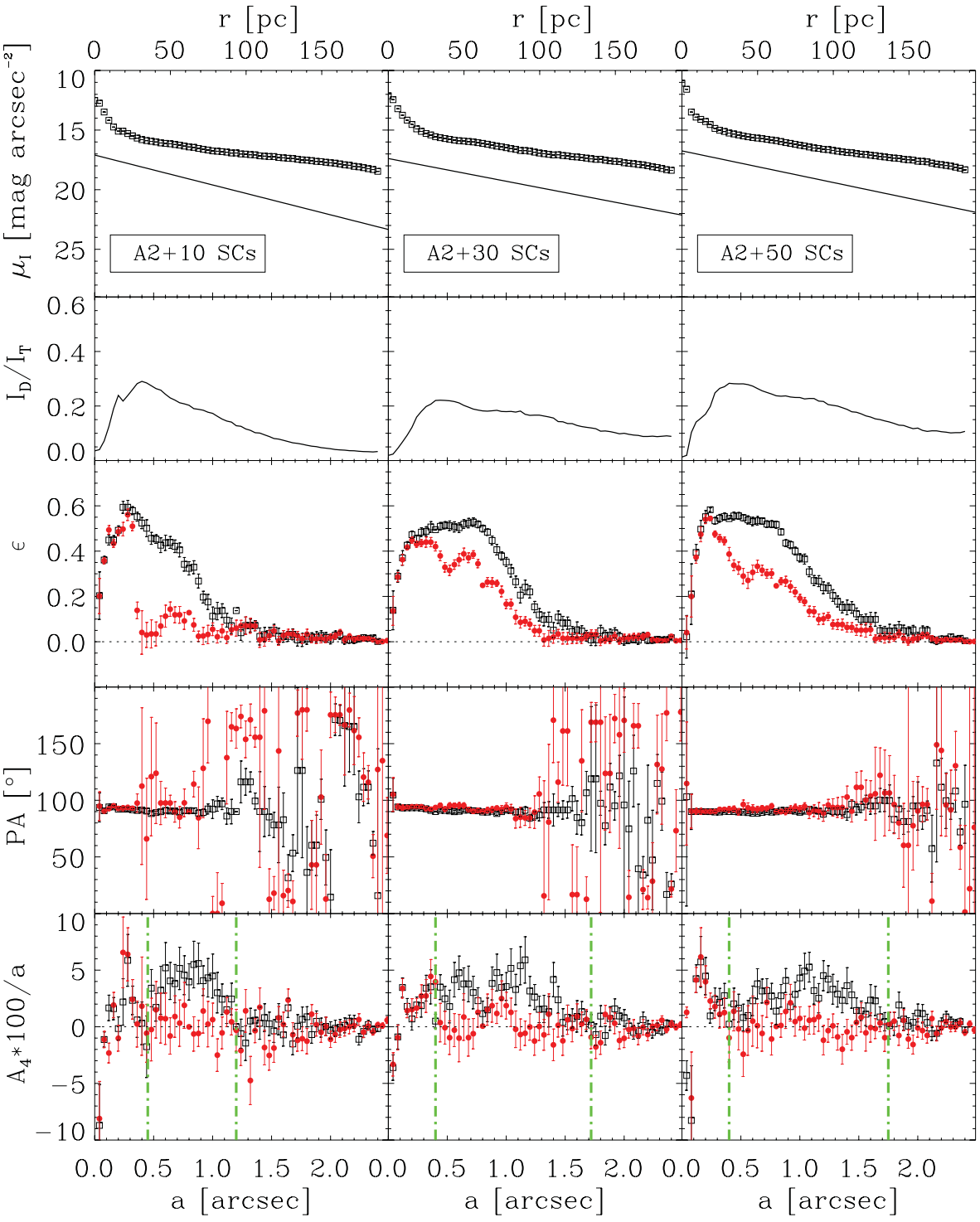

Figure 4. Isophotal parameters of the nuclear region of model A2 as a function of the isophotal semimajor axis based on the analysis of the surface brightness distribution measured in the mock images obtained after the accretion of 10 (left-hand panels), 30 (central panels) and 50 (right-hand panels) star clusters. From top to bottom: surface brightness radial profiles of the galaxy (open black squares) and NSD (solid line), radial profiles of the NSD-to-total surface brightness ratio, radial profiles of the galaxy ellipticity, PA and fourth cosine Fourier coefficient before (open black squares) and after (filled red circles) the subtraction of the best-fitting model for the NSD. The vertical (green) dot–dashed lines mark the radial range within which the light distribution is characterized by discy isophotes ($A_4 > 0$) due to the presence of the NSD.

Pizzella et al. 2002; Krajnović & Jaffe 2004; Morelli et al. 2010). We do not apply any deconvolution to our mock WFC3/UVIS images since they have not been convolved with any PSF to begin with.

The remaining NSD parameters are adjusted until the departures from perfect ellipses are minimized (i.e. $A_4 \simeq 0$ over all the observed radial range). For each disc model, first we obtain the disc-free image of the galaxy by subtracting the disc model from the galaxy

Table 2. Photometric parameters of the NSDs derived from the photometric decomposition of the mock images of model A2.

N_{SC}	Fit	$\mu_{0,I}$ (mag arcsec^{-2})	h (arcsec)	i (°)	$L_{T,I}$ (10^6 L$_\odot$)
10	SB	$17.09^{+0.03}_{-0.11}$	$0.43^{+0.02}_{-0.04}$	$75.5^{+1.5}_{-1.9}$	$4.7^{+0.1}_{-0.5}$
10	EF	16.92 ± 0.20	0.40 ± 0.04	77.9 ± 1.4	$3.8^{+0.5}_{-1.0}$
30	SB	$17.39^{+0.31}_{-0.14}$	$0.54^{+0.08}_{-0.12}$	$78.3^{+2.3}_{-3.3}$	$4.6^{+1.2}_{-0.6}$
30	EF	17.11 ± 0.20	0.52 ± 0.04	76.7 ± 0.8	$6.8^{+1.3}_{-1.2}$
50	SB	$16.94^{+0.19}_{-0.15}$	$0.52^{+0.07}_{-0.08}$	$78.1^{+3.1}_{-2.8}$	6.5 ± 1.0
50	EF	16.85 ± 0.10	0.54 ± 0.04	77.3 ± 0.6	7.6 ± 0.7

Note. Column (1): number of accreted star clusters. Column (2): photometric decomposition method: SB = Scorza–Bender method on the mock images including the light contribution of the bulge, EF = exponential fit on the mock images excluding the light contribution of the bulge. Column (3): observed central surface brightness. Column (4): scalelength. Column (5): inclination. Column (6): total I-band luminosity.

image. Then, we perform an isophotal analysis of the disc-free image using ELLIPSE. We calculate

$$\chi^2 = \sum_{i=1}^{N} \frac{A^2_{4,\mathrm{disc-free}}(i)}{\sigma^2(i)}, \quad (3)$$

where $A_{4,\,\mathrm{disc\text{-}free}}(i)$ is the value of the A_4 Fourier coefficient measured for the ith isophote in the disc-free image, and N is the total number of fitted isophotes. We assume $\sigma(i) = 0.01$ as a typical error on $A_{4,\,\mathrm{disc\text{-}free}}$ for all the isophotes in the region of the NSD. The NSD region is bracketed by two vertical lines in Fig. 4. The minimum value of χ^2 corresponds to the best-fitting model of the NSD. We determine $\Delta\chi^2 \equiv \chi^2 - \chi^2_{\mathrm{min}}$ and derive its confidence levels under the assumption that the errors are normally distributed. The resulting contour plots of χ^2 allow us to derive the best-fitting values of I_0, h, and q, and their 3σ uncertainties. The inclination is calculated as $i = \arccos q$. The resulting values of the observed central surface brightness, scalelength, inclination and total luminosity of the NSD in the I-band for the different time-steps of model A2 are listed in Table 2.

We test our decompositions by an independent analysis of an image which excludes all bulge particles. We build an I-band image of each time-step with the same assumptions as in Section 3.1 including only the light contribution of the bare NCD and accreted star clusters, which are expected to be the building blocks of the NSD. The resulting surface brightness distribution is modelled with a Sérsic component and an exponential disc by applying the two-dimensional fitting algorithm GALFIT (Peng et al. 2002). The Sérsic component accounts for the central bright structure which dominates the light distribution in the innermost 0.2 arcsec (Fig. 4). The best-fitting parameters of the exponential disc are in agreement within errors with the NSD parameters we derived with the Scorza–Bender method, as shown in Table 2.

We also applied the Scorza–Bender method to model A1. In this case, it failed to find a reasonable NSD, with the best model having a scalelength $h = 0$ pc.

3.4 Rotation parameter

We compute the rotation parameter as

$$\frac{V}{\sigma} = \sqrt{\frac{\langle V^2 \rangle}{\langle \sigma^2 \rangle}} = \sqrt{\frac{\Sigma_{n=1}^{N} F_n V_n^2}{\Sigma_{n=1}^{N} F_n \sigma_n^2}}, \quad (4)$$

Table 3. Kinematic parameters of the nuclear elongated structure observed in models A1 and A2.

Model	N_{SC}	$\frac{M_{SC}}{M_{in}}$	V (km s^{-1})	σ (km s^{-1})	$\frac{V}{\sigma}$	ϵ	$\left(\frac{V}{\sigma}\right)^*$
A1	10	3	15.1	15.7	0.95	0.65	0.70
A1	20	6	15.7	19.4	0.80	0.62	0.63
A1	27	8.1	16.7	21.8	0.77	0.60	0.63
A2	10	2	12.6	7.6	1.66	0.75	0.96
A2	30	6	14.2	11.0	1.29	0.68	0.82
A2	50	10	18.5	13.8	1.34	0.72	0.84

Note. Column (1): model number. Column (2): number of accreted star clusters. Column (3): ratio of the accreted mass to initial mass of the nuclear star cluster. Columns (4) and (5): luminosity-weighted velocity and velocity dispersion excluding the contribution of the central pre-existing structure. Column (6): rotation parameter. Column (7): luminosity-weighted ellipticity. Column (8): ratio of V/σ to the value predicted for an edge-on oblate isotropic rotator with an intrinsic ellipticity given in Column (7) and flattened by rotation.

and the mean ellipticity as

$$\epsilon = 1 - q = 1 - \sqrt{\frac{\langle y^2 \rangle}{\langle x^2 \rangle}} = 1 - \sqrt{\frac{\Sigma_{n=1}^{N} F_n y_n^2}{\Sigma_{n=1}^{N} F_n x_n^2}}, \quad (5)$$

where q is the axis ratio and, following H11, V_n, σ_n and F_n are the line-of-sight velocity, velocity dispersion, and flux of the pixel at (x_n, y_n), respectively. The origin of the Cartesian coordinates (x, y) is at the centre of the galaxy, with the x-axis aligned with the line of nodes. We consider only the N pixels between 15 and 40 pc from the galaxy centre to calculate the luminosity-weighted values of $\langle V^2 \rangle$, $\langle \sigma^2 \rangle$, $\langle x^2 \rangle$ and $\langle y^2 \rangle$ in order to exclude the contribution of the pre-existing nuclear structure (i.e. the NCS in model A1 and the NCD in model A2). There is no need to correct for inclination, since the kinematic maps are built with the simulated galaxies edge-on. We also derive the ratio, $(V/\sigma)^*$, of the measured V/σ to the value predicted for an edge-on, isotropic oblate system flatted by rotation with the same intrinsic ellipticity as the elongated structure (see Kormendy & Illingworth 1982).

The resulting values of the luminosity-weighted velocity, velocity dispersion and ellipticity together with the rotation parameter (V/σ) and $(V/\sigma)^*$ for all time-steps are listed in Table 3. The axis ratio of the elongated structure measured in the nucleus of model A1 is $q \simeq 0.4$. The stellar kinematics and ellipticity are therefore consistent with an anisotropic rotator with $(V/\sigma)^* \simeq 0.6$. The elongated structure of model A2 ($q \simeq 0.3$) instead rotates almost as fast as an isotropic oblate system, $(V/\sigma)^* \simeq 0.8$. In both models, V and σ increase with the number of accreted star clusters, although the difference between the values measured in the first and last time-step is smaller than the typical 1σ error (5–10 km s^{-1}) on the stellar kinematics measured in galactic nuclei (e.g. Emsellem et al. 2004).

4 DISCUSSION

From the analysis of the unsharp masked image, the nucleus in model A1 shows an elongated structure (Fig. 2, left-hand panels). Its radial extent increases with the number of accreted star clusters as seen from the increase of the radial range where significantly elongated isophotes are measured (Fig. 3). Indeed, $\epsilon > 0$ out to 1.1, 2.1 and 2.4 arcsec from the centre after the accretion of 10, 20 and 27 star clusters. In all the time-steps, the ellipticity peaks at $\epsilon_{\mathrm{max}} \simeq 0.6$ at about 0.2 arcsec (15 pc), where the NCS dominates,

as shown in the analysis of H11, and it gently decreases outwards. The absence of a sharp peak in the A_4 radial profile at the location where NSDs reside is the main photometric reason for concluding that no NSD is present, even if the unsharp mask technique shows an elongated structure. Such feature can also be caused by isophotes of increasing ellipticity inwards. Therefore, unveiling an NSD requires performing a detailed measurement of the surface brightness distribution in the nuclear regions. In addition, the rotation parameter and ellipticity measured from the stellar kinematics are consistent with an anisotropic rotation (Table 3). Therefore, we conclude that the elongated nuclear structure observed in model A1 is not an NSD, in spite of the fact that the total accreted mass, 1.6×10^7 $M_\odot$, is comparable to that of observed NSDs (e.g. Morelli et al. 2004).

On the other hand, the photometric and kinematic properties of the nuclear structure seen in model A2 (Fig. 2, right-hand panels) are reminiscent of an NSD. The rising ellipticity is associated with discy isophotes over a radial range which steadily increases with the number of accreted star clusters (Fig. 4). The ellipticity peaks at a similar value as model A1 ($\epsilon_{\rm max} \simeq 0.6$) although it is $\epsilon \simeq 0.5$ over a wider radial range (0.2–0.8 arcsec). At larger radii, the isophotes quickly become round. The elongated structure rotates as fast as an oblate isotropic spheroid (Table 3). Its surface brightness distribution can be modelled as an inclined exponential disc with a maximum local light contribution to the total surface brightness of about 30 per cent at 0.4 arcsec from the centre. The NSD parameters measured in the three time-steps are consistent with each other within the errors. Their mean values from the Scorza–Bender method are $\mu_{0,I} = 17.14$ mag arcsec^{-2}, $h = 0.50$ arcsec (38.8 pc) and $i = 77.^\circ3$ corresponding to $L_{{\rm T},I} = 5.3 \times 10^6$ $L_\odot$. The inclination and PA of the line of nodes of the NSD and its host bulge are the same within the errors. The total accreted mass is 1.0×10^7 $M_\odot$ and it is consistent with that of observed NSDs.

We compared the structural properties of the NSD of model A2 to those of the known NSDs (Ledo et al. 2010; Corsini et al. 2012). We derive the Johnson V-band central surface brightness of the model NSD from the mean I-band value using the IRAF task SYNPHOT. Because this correction depends on the galaxy spectral energy distribution, it is calculated using the spectral template for an Sc spiral galaxy by Kinney et al. (1996) to match the late morphological type of NGC 4244. The resulting shift is $V - I = 1.46$. The mean observed central surface brightness is corrected for mean inclination as

$$\mu^0_{0,V} = \mu_{0,V} - 2.5\log(\cos i) = 20.24 \text{ mag arcsec}^{-2}. \quad (6)$$

The scalelength and face-on central surface brightness are close to those of the larger observed NSDs and fit on the $\mu^0_{0,V} - h$ relation for galaxy discs, as we show in Fig. 5.

We also compare the total luminosity of the NSD with that predicted by extrapolating the I-band Tully–Fisher relation (Masters et al. 2006, Fig. 6) to discs of similar rotational velocity ($\sim$20 km s^{-1}). We assume the rotation width of the NSD to be $W = 2\langle V_{\rm rms}\rangle$, where the luminosity-weighted second-order kinematic moment $\langle V_{\rm rms}\rangle = \sqrt{\langle V^2\rangle + \langle\sigma^2\rangle}$ is measured from the kinematic maps of the simulated galaxy excluding the light contribution of the bulge (Table 1). We find that the rotation width and luminosity of the NSD of model A2 are consistent with the Tully–Fisher relation. Similarly, we measure the rotational width for the NSDs for which both the stellar kinematics and photometric decomposition are available so far (NGC 4458 and NGC 4478: kinematics from Halliday et al. 2001 and photometry from Morelli et al. 2004;

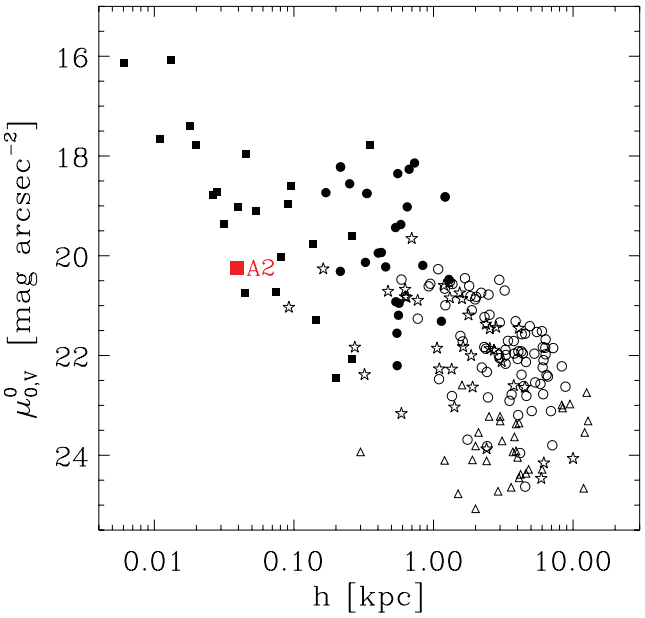

Figure 5. The face-on central surface brightness as a function of disc scalelength adapted from Ledo et al. (2010) and including the NSD of NGC 4698 (Corsini et al. 2012). The large red square marks the NSD of model A2. Open circles indicate high surface brightness spirals, triangles low surface brightness spirals, stars show S0s, and filled circles discy ellipticals. Small squares represent observed NSDs.

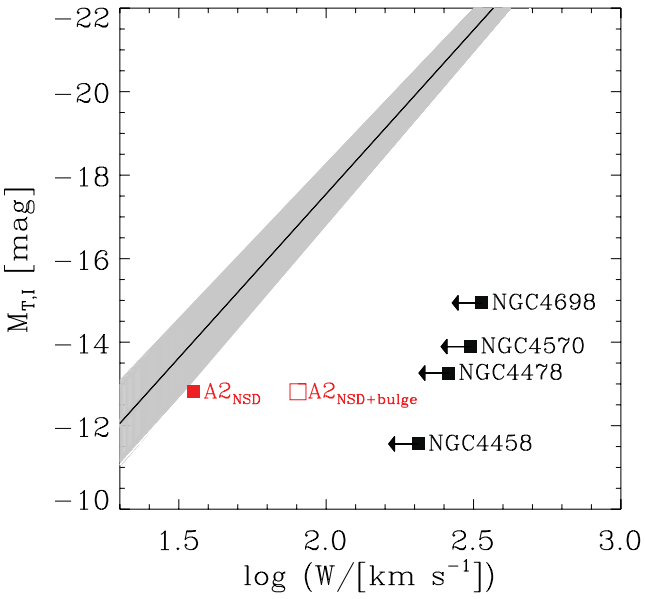

Figure 6. The total magnitude as a function of the rotation width for the NSDs observed in real galaxies (black squares) and in the nucleus of model A2 (red squares). Only observed NSDs with both measured kinematics and photometric decomposition are shown. The two values for model A2 are derived by excluding (filled red square) and including (open red square) the bulge contribution. The solid line and the grey region correspond to the Tully–Fisher relation in the I band by Masters et al. (2006) and its scatter, respectively.

NGC 4570: kinematics from Krajnović & Jaffe 2004 and photometry from Morelli et al. 2010; NGC 4698: kinematics from Bertola et al. 1999 and photometry from Corsini et al. 2012). Their luminosities are offset below the Tully–Fisher relation in agreement with

the earlier findings of Morelli et al. (2004). The NSDs in real and simulated galaxies show a different behaviour in the Tully–Fisher relation in spite of having similar luminosities and similar maximum light contributions (Fig. 6). We explain the discrepancy as due to the fact that for real galaxies observations miss a proper decomposition of the line-of-sight velocity distribution. The rotation widths of NSDs in real galaxies are overestimated due to the contribution of the host spheroid to the kinematics (in particular to the velocity dispersion) measured in the nuclear regions. This is not the case of the NSD of model A2 where we have the actual kinematics of the nuclear disc, making the comparison with the Tully–Fisher prediction straightforward. Its rotational width increases and the NSD drops below the Tully–Fisher relation if the measured stellar kinematics includes the bulge contribution. However, then the rotational width ($\simeq 80\,\mathrm{km\,s^{-1}}$) is not as large as in the observed NSDs ($\simeq 230\,\mathrm{km\,s^{-1}}$) since its bulge has a lower velocity dispersion compared to the larger spheroidal component of the early-type galaxies hosting the NSDs shown in Fig. 6.

5 CONCLUSIONS

We have analysed two *N*-body simulations from H11 exploring the dissipationless merging of multiple star clusters into the centre of a galaxy. The simulations were originally aimed at investigating the photometric, kinematic and dynamic properties of the nucleus of NGC 4244 which hosts a massive stellar cluster in rapid rotation (Seth et al. 2006, 2008). In this paper, we have investigated the images and kinematic maps built from the simulation as if they were real, assuming the galaxy to be at the distance of the Virgo cluster. We have tested the importance of purely stellar dynamical mergers for the formation and growth of NSDs by looking for their presence in the nucleus of the simulated galaxies. Our main conclusions can be summarized as follows.

(i) A flattened merger remnant ($q \simeq 0.3$–0.4) with a radius of about 100 pc is observed in the nucleus of the simulated galaxy when a few tens of star clusters with sizes and masses comparable to those of globular clusters observed in the Milky Way are accreted on to a pre-existing stellar component at the centre. This flattened structure forms regardless of whether the pre-existing component is a massive spherical cluster (as is the NCS of model A1) or a rapidly rotating disc (as is the NCD of model A2) and regardless of the amount of accreted mass ($2-10$ times) with respect to the mass of the pre-existing component ($\sim 10^6\,\mathrm{M_\odot}$).

(ii) The merger remnant passes all observational constraints to be an NSD when the star clusters are accreted on to a pre-existing NCD. The structural parameters of the NSD were obtained by applying the same photometric decomposition adopted for real galaxies based on the analysis of isophotal shapes. The photometric and kinematic properties of the NSD in the simulated galaxy are remarkably similar to those of NSDs observed in the nuclei of real galaxies. In particular, the scalelength (38.8 pc) and face-on central surface brightness (20.24 $V\,\mathrm{mag\,arcsec^{-2}}$) fit on the $\mu^0_{0,V} - h$ relation for galaxy discs. The total luminosity ($5.3 \times 10^6\,\mathrm{L_\odot}$) is consistent with that predicted by extrapolating the *I*-band Tully–Fisher relation to discs of similar rotational width ($\sim 40\,\mathrm{km\,s^{-1}}$). The mass of the NSD ($\sim 1 \times 10^7\,\mathrm{M_\odot}$) is close to that of the few NSDs for which it has been measured.

(iii) The independent analysis performed by fitting an exponential disc to the surface brightness distribution after excluding the light from the bulge finds best-fitting disc parameters in agreement with those derived with the Scorza–Bender method, showing that the latter is robust. The elongated structures found in the unsharp images are not sufficient proof of the presence of an NSD: the same feature can also be caused by isophotes of increasing inwards ellipticity at small radii. Therefore, to unveil an NSD, performing a detailed measurement of the surface brightness distribution in the nuclear regions is necessary and the Scorza–Bender decomposition method is a robust way of doing this.

(iv) The purely stellar dynamical merger of star clusters on to the centre of a galaxy is a viable mechanism for growing an NSD. This shows that most of its mass (up to 70–90 per cent) can be assembled from already formed stars through the migration and accretion of star clusters on to the galactic centre.

ACKNOWLEDGEMENTS

EP acknowledges the Jeremiah Horrocks Institute of the University of Central Lancashire in Preston, UK, for the hospitality while this paper was in progress. EP is partially supported by Fondazione Angelo Della Riccia. LM acknowledges Padua University grant CPS0204. This work was supported by Padua University through the grants 60A02-1283/10, 5052/11 and 4807/12. VPD is supported in part by STFC Consolidated grant # ST/J001341/1. Simulations in this paper were performed on the COSMOS Consortium supercomputer within the DIRAC Facility jointly funded by STFC, the Large Facilities Capital Fund of BIS and the High Performance Computer Facility at the University of Central Lancashire.

REFERENCES

Agarwal M., Milosavljević M., 2011, ApJ, 729, 35
Antonini F., 2013, ApJ, 763, 62
Antonini F., Capuzzo-Dolcetta R., Mastrobuono-Battisti A., Merritt D., 2012, ApJ, 750, 111
Bekki K., 2007, Publ. Astron. Soc. Aust., 24, 77
Bender R., Doebereiner S., Moellenhoff C., 1988, A&AS, 74, 385
Bertola F., Corsini E. M., 1999, in Barnes J. E., Sanders D. B., eds, Proc. IAU Symp. 186, Galaxy Interactions at Low and High Redshift. Kluwer, Dordrecht, p. 149
Bertola F., Corsini E. M., Vega Beltrán J. C., Pizzella A., Sarzi M., Cappellari M., Funes J. G., 1999, ApJ, 519, L127
Capuzzo-Dolcetta R., 1993, ApJ, 415, 616
Capuzzo-Dolcetta R., Miocchi P., 2008a, ApJ, 388, 69
Capuzzo-Dolcetta R., Miocchi P., 2008b, ApJ, 681, 1136
Corsini E. M. et al., 1999, A&A, 342, 671
Corsini E. M., Méndez-Abreu J., Pastorello N., Dalla Bontà E., Morelli L., Beifiori A., Pizzella A., Bertola F., 2012, MNRAS, 423, L79
Cretton N., van den Bosch F. C., 1999, ApJ, 514, 704
De Lorenzi F., Hartmann M., Debattista V. P., Seth A. C., Gerhard O., 2013, MNRAS, 429, 2974
Debattista V. P., Sellwood J. A., 2000, ApJ, 543, 704
Dressel L., 2011, WFC3 Instrument Handbook, Version 4.0. STScI, Baltimore
Emsellem E., van de Ven G., 2008, ApJ, 674, 653
Emsellem E. et al., 2004, MNRAS, 352, 721
Falcón-Barroso J. et al., 2004, MNRAS, 350, 35
Ferrarese L. et al., 2006, ApJ, 644, L21
Figer D. F., McLean I. S., Morris M., 1999, ApJ, 514, 202
Figer D. F. et al., 2002, ApJ, 581, 258
Halliday C., Davies R. L., Kuntschner H., Birkinshaw M., Bender R., Saglia R. P., Baggley G., 2001, MNRAS, 326, 473
Hartmann M., Debattista V. P., Seth A., Cappellari M., Quinn T. R., 2011, MNRAS, 418, 2697 (H11)
Hernquist L., 1990, ApJ, 356, 359
Jedrzejewski R. I., 1987, MNRAS, 226, 747

Kinney A. L., Calzetti D., Bohlin R. C., McQuade K., Storchi-Bergmann T., Schmitt H. R., 1996, ApJ, 467, 38
Kormendy J., Illingworth G., 1982, ApJ, 256, 460
Kormendy J., Dressler A., Byun Y. I., Faber S. M., Grillmair C., Lauer T. R., Richstone D., Tremaine S., 1994, in Meylan G., Prugniel P., eds, Proc. ESO/OHP Workshop, Dwarf galaxies. ESO, Garching, p. 147
Kormendy J., Gebhardt K., Fisher D. B., Drory N., Macchetto F. D., Sparks W. B., 2005, AJ, 129, 2636
Krajnović D., Jaffe W., 2004, A&A, 428, 877
Ledo H. R., Sarzi M., Dotti M., Khochfar S., Morelli L., 2010, MNRAS, 407, 969
Lotz J. M., Telford R., Ferguson H. C., Miller B. W., Stiavelli M., Mack J., 2001, ApJ, 552, 572
Magorrian J., 1999, MNRAS, 302, 530
Maraston C., 1998, MNRAS, 300, 872
Maraston C., 2005, MNRAS, 362, 799
Masters K. L., Springob C. M., Haynes M. P., Giovanelli R., 2006, AJ, 653, 880
Milosavljević M., 2004, ApJ, 605, L13
Morelli L. et al., 2004, MNRAS, 354, 753
Morelli L., Cesetti M., Corsini E. M., Pizzella A., Dalla Bontà E., Sarzi M., Bertola F., 2010, A&A, 518, A32
Peng C. Y., Ho L. C., Impey C. D., Rix H.-W., 2002, AJ, 124, 266
Pizzella A., Corsini E. M., Morelli L., Sarzi M., Scarlata C., Stiavelli M., Bertola F., 2002, ApJ, 573, 131
Rix H. W., White S. D. M., 1990, ApJ, 362, 52
Scorza C., Bender R., 1995, A&A, 293, 20
Scorza C., van den Bosch F. C., 1998, MNRAS, 300, 469
Seifert W., Scorza C., 1996, A&A, 310, 75
Sellwood J. A., 2008, ApJ, 679, 379
Seth A. C., Dalcanton J. J., Hodge P. W., Debattista V. P., 2006, AJ, 132, 2539
Seth A. C., Blum R. D., Bastian N., Caldwell N., Debattista V. P., 2008, ApJ, 687, 997
Shlosman I., Begelman M. C., 1989, ApJ, 341, 685
Sil'chenko O. K., 1997, Astron. Rep., 41, 567
Tremaine S. D., Ostriker J. P., Spitzer L., Jr, 1975, ApJ, 196, 407
van den Bosch F. C., 1998, ApJ, 507, 601
van den Bosch F. C., de Zeeuw P. T., 1996, MNRAS, 283, 381
van den Bosch F. C., Emsellem E., 1998, MNRAS, 298, 267
van den Bosch F. C., Jaffe W., van der Marel R. P., 1998, ApJ, 293, 343

This paper has been typeset from a TEX/LATEX file prepared by the author.